MDPI

Article

Superhydrophobic Epoxy/Fluorosilicone/PTFE Coatings Prepared by One-Step Spraying for Enhanced Anti-Icing Performance

Lei Fan [1,2], Bo Li [1], Yan Wang [3], Jinhang He [1], Jie Bai [1], Tao Zhu [2] and Yuan Yuan [2,*]

[1] Institute of Electric Power Science of Guizhou Power Grid Co., Ltd., Guiyang 550005, China
[2] College of Materials Science and Engineering, Chongqing University, Chongqing 400044, China
[3] Guiyang Power Supply Bureau of Guizhou Power Grid Co., Ltd., Guiyang 550001, China
* Correspondence: yuany@cqu.edu.cn

Abstract: The icing of glass insulators is likely to cause faults such as insulator flashover, which poses a serious threat to the power system. Traditional deicing techniques have the disadvantage of being costly and inefficient. Herein, polytetrafluoroethylenes (PTFEs) as nanoparticles and epoxy and fluorosilicone resins as binders were blended to construct an anti-icing coating. The superhydrophobic (SHP) epoxy/fluorosilicone/PTFE coatings for anti-icing were successfully prepared on glass slides through one-step spraying. The effect of PTFE mass fraction on the microstructure, on the wettability and on the anti-icing properties of the coatings was investigated. The results showed that the coatings with different PTFE mass fractions had different microstructures. When the PTFE mass fraction was 47.2%, the SHP coating exhibited a uniform rough structure with an apparent contact angle as high as 164.7° and a sliding angle as low as 3.2°. Moreover, the water droplets can bounce back five times with a contact time of only 9.5 ms and a rebound height of 4.58 mm. In the low-temperature environment (−10 °C), the SHP coating displayed good anti-frosting, anti-icing and icephobic properties. The delayed frosting time (1499 s) and delayed freezing time (1295.3 s) of the SHP coating were three and five times longer than those of the glass, respectively. The SHP coating presented an ice-adhesion strength (39.8 kPa) that was six times lower than that of glass. The prepared SHP coating demonstrated potential applications for the anti-icing of glass insulators.

Keywords: superhydrophobic; PTFE; spraying; anti-icing

1. Introduction

Icing is a common natural phenomenon. Transmission lines passing through high-altitude areas are highly susceptible to icing in cold and complex environments [1]. Ice accumulation on transmission lines often causes conductor dancing and insulator flashover, and it can even lead to accidents such as conductor breakage and tower collapse, which seriously affect the stable operation of power systems [2–4]. Traditional deicing methods, including high-current ice melting, have certain deicing effects, but there are problems, such as its requiring complex equipment, its high price and its low efficiency [5–7]. The anti-icing of transmission lines is not only a study hot spot for researchers but also an urgent problem to be solved in the power system. Therefore, it is of great significance to develop a simple and effective anti-icing technology for the safe operation of transmission lines.

Inspired by the lotus leaf effect in nature, biomimetic SHP coatings with excellent water repellency and self-cleaning properties have received a lot of attention and are often used in anti-fouling [8], anti-corrosion [9] and self-cleaning [10] applications and for oil–water separation [11]. An SHP coating is also considered as a potential anti-icing method. The excellent hydrophobicity allows supercooled water droplets in a low-temperature environment to roll away from the SHP surface before freezing, which reduces the possibility of water droplets' freezing [12,13]. Furthermore, the rough structure of the SHP surface can reduce the contact area of ice with the surface. The formed air cushion can effectively

decrease the ice-adhesion strength and facilitate the deicing of the material [14,15]. On the other hand, it is important to emphasize that SHP surfaces are not always icephobic [16,17]. In low-temperature and high-humidity environments, the water-repellent properties of SHP surfaces are prone to be lost. Moreover, the rough structure is easily invaded by water vapor and increases the ice-adhesion strength of SHP surfaces. All these are not conducive to the anti-icing of the surface. At the same time, using a slippery liquid-infused porous surface (SLIPS) is proposed to solve the problem of SHP coating failures [18,19]. The lubricant layer on the surface can isolate water vapor and substantially reduce the ice-adhesion strength. However, the lubricant on the surface of SLIPSs not only is easy to lose but also may pollute the environment.

Compared with SLIPS, the preparation of SHP coatings does not require exhaustive efforts to complete the infusion of lubricant. In addition, the rough structure of SHP coatings is more favorable to resisting external damage than the lubricant of SLIPS. In summary, SHP coatings with superhydrophobic properties still have potential applications in the field of anti-icing [12–15,20,21]. In general, SHP surfaces with contact angles higher than 150° and sliding angles lower than 10° can be prepared by constructing rough structures, combined with low-surface-energy modifications [22,23]. At present, methods commonly used to prepare SHP surfaces include self-assembly [24], laser engraving [25], chemical etching [26] and magnetron sputtering [27]. The SHP surfaces prepared using the above methods have good anti-icing properties. However, these methods [24–27] often require complex manufacturing processes and expensive equipment, making it difficult to achieve large-scale industrial production.

In contrast, spraying, as a simple and efficient technique, can significantly decrease the cost of coating preparation. The spraying method can reasonably simplify the preparation process of the coating and is commonly used for the batch production of complexly shaped components [28,29]. The SHP coatings [30–33] prepared by spraying still exhibited promising anti-icing properties in low-temperature (below 0 °C) environments. In −4 and −8 °C environments, the SHP coating retained good water-repellent properties, and the water droplets rapidly rolled off the surface [30]. The freezing point of water droplets was reduced by the SHP coating, leading to a delayed icing process in the condensing environment [31]. In addition, the anti-icing performance of SHP coatings was significantly influenced by the mass fraction of the filler. SHP coatings with 30% of the mass fraction of MWCNT displayed the best delayed icing performance (no ice residue on the surface within 30 min) in a −10 °C environment [32]. In a −20 °C environment, the SHP coatings of carbon fiber/epoxy composites prepared by combining spraying with hard-template hot pressing showed an icing delay time of up to 640 s and an icing-adhesion strength down to 50 kPa [33].

However, the current research still suffers from requiring cumbersome processes [29,33–35] and expensive materials [32,34]. All these may limit its wide application in industry. In order to be suitable for industrial production, the steps for preparing SHP coatings by spraying should be more simplified, and the materials used should be cheaper and more readily available. Most of the substrates used for the anti-icing SHP coatings prepared by the abovementioned spraying methods [29,31,32,34] are metallic materials. There are few studies on nonmetallic materials (such as glass) [30]. In contrast, in addition to transmission aluminum conductors, glass insulators are also important components widely used in transmission lines [28,36]. The icing of glass insulators can lead to a dramatic decrease in the electrical insulation properties of insulators, which causes a serious threat to the operation of power systems [3,4,37–39]. Furthermore, glass insulators in harsh low-temperature environments are prone not only to icing but also to frost formation on the surface. The formed frost crystals will intensify the ice accumulation [40–42], which will in turn interfere with the normal operation of the power grid. Therefore, it is necessary to study the anti-frosting, anti-icing and icephobic properties of SHP coatings on the basis of using glass to maintain the normal electrical insulation performance of glass insulators.

In this work, epoxy/fluorosilicone/PTFE coatings were prepared on glass slides by using one-step spraying. The microscopic morphology and chemical composition of the coatings were characterized. The wettability, anti-frosting, anti-icing and icephobic properties of the coatings were evaluated. The relationship between the microstructure, wettability and anti-icing performance of the coatings was investigated. The mechanism of the anti-frosting, anti-icing and icephobic of SHP coatings was discussed, and a schematic diagram of the mechanism was constructed. Importantly, techniques such as laser engraving [24–27] require very expensive equipment to produce SHP coatings. The SHP anti-icing coatings prepared using spraying always consume costly materials and require the investment of a lot of workforce resources [29,32–35].

The materials used in this work, however, are cheap and easily available common products. Therefore, the SHP coating prepared by one-step spraying has high cost-effectiveness as a potential application in the anti-icing of glass insulators. In addition, the SHP coating prepared on glass in this work demonstrated superior anti-icing properties to the reported coatings prepared on metals [31–33]. Among them, the freezing time was significantly prolonged and the ice-adhesion strength was also reduced. In particular, the prepared coatings were accompanied by good anti-frosting properties, which were not previously reported in the literature [30–33]. The icing–deicing cycle tests indicated that the SHP coating needed further improvement in its anti-icing durability. This study provides a more comprehensive experimental reference for the preparation of anti-icing coatings on glass insulators.

2. Materials and Methods

2.1. Materials

The epoxy resin (GCC135) and curing agent were purchased from Kunshan Lvxun Chemicals Industry Co., Ltd. The epoxy resin is composed mainly of bisphenol A epoxy resin and ethylene glycol diglycidyl ether. The main component of the curing agent is modified isophorone diamine. Fluorosilicone resin was supplied by Chengdu Aikeda Chemical Reagent Co., Ltd., and its fluorine content was greater than 26%. Polytetrafluoroethylene (PTFE) powder with an average particle size of 200 nm was obtained from Shanghai Macklin Biochemical Co., Ltd. 1H, 1H, 2H, 2H heptadecafluorodecyltrimethoxy silane (FAS-17) was provided by Shanghai Aladdin Biochemical Technology Co., Ltd. The ethyl acetate and anhydrous ethanol were supplied by Chengdu Kelong Chemical Co., Ltd. and Chongqing Chuandong Chemical (Group) Co., Ltd., respectively. Glass slides (7101) were purchased as substrates from Jiangsu Feizhou Glass Plastic Co., Ltd. All reagents were analytical grade reagents and could be used without further purification.

2.2. Preparation of Coatings

The coating was prepared using one-step spraying, and the preparation process is shown in Figure 1. First, 25 g of ethyl acetate, 3 g of fluorosilicone resin, 2 g of epoxy resin and 0.5 g of FAS-17 were put into a beaker and stirred on a magnetic stirrer for 30 min. After adding different masses of PTFE powder, magnetic stirring and ultrasonic dispersion were performed for 10 min each. Next, 0.6 g of curing agent for epoxy resin was added and stirred magnetically for 10 min to obtain a well-mixed homogeneous solution. The speed of magnetic stirring was 400 r/min. Before spraying, glass slides were ultrasonically cleaned in absolute ethanol for 10 min and deionized water for 10 min, separately. To prepare coatings with PTFE mass fractions of 0%, 15.2%, 34.9%, 47.2% and 58.8%, the mass of PTFE powder added was controlled to be 0, 1, 3, 5 and 8 g, respectively. The uniformly mixed solution was poured into the spray bottle, and the spray gun was aimed at the vertically placed slides for one-step spraying. The nozzle diameter was 1.5 mm, the spraying pressure was controlled at 0.2 MPa, and the spraying distance was kept at 15 cm. For uniform spraying, the spray gun was slowly moved from top to bottom. The sprayed coating was first cured at room temperature for 1 h and then placed in a drying oven overnight.
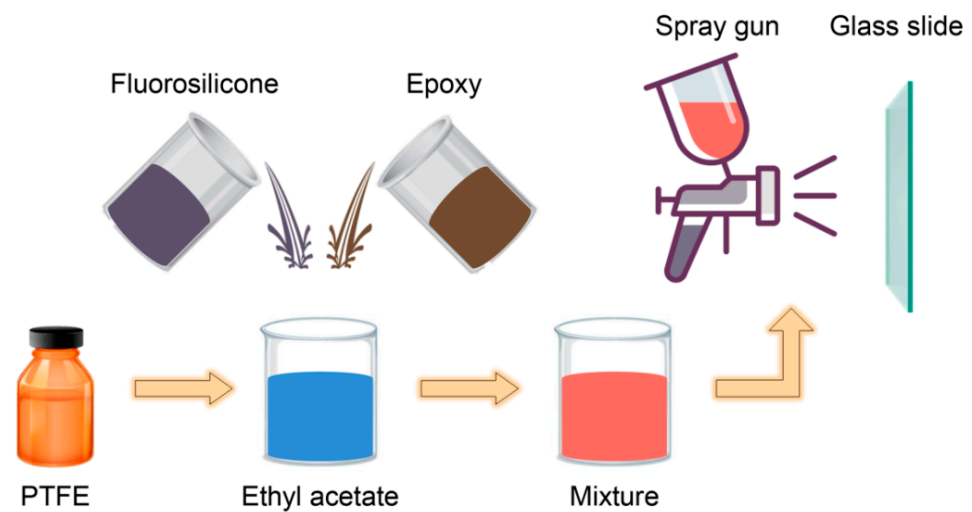
Figure 1. Preparation of superhydrophobic coating by one-step spraying.

2.3. Measurements and Characterization

Scanning electron microscopy (SEM, Zeiss Auriga, Jena, Germany) and energy-dispersive spectroscopy (EDS) were used to characterize the microscopic morphology and elemental composition of the coatings. A Fourier transform infrared spectrometer (FTIRS, Nicolet iS10, Waltham, MA, USA) was employed to detect the chemical composition of the coatings. A water contact angle meter (SINDIN SDC-300) was applied to measure the apparent contact angle (CA) and sliding angle (SA) of the coatings. The water-droplet-bouncing performance was evaluated using ahigh-speed camera (M220, Revealer, Hefei, China). The volume of a water droplet was about 6 μL, and five random locations were measured and averaged as the test results.

Frosting, water-droplet-freezing and ice-adhesion-strength tests were conducted separately by using a semiconductor cooling platform. During the tests, the ambient temperature and humidity were maintained at 25 °C and 50%, respectively. The coating was horizontally placed on a Peltier cooling plate, and the temperature of the cooling plate was lowered from 25 to −10 °C. The frosting of the coating was photographed at intervals by using a cell phone camera.

Deionized water (6 μL) was dropped onto the surface of the coating. The temperature of the cooling plate was lowered to −10 °C. Images of frozen water droplets were collected in real time by using a water contact angle meter until the water droplets were completely frozen. The freezing of the water droplets can be inferred from the transparency and shape of the water droplets in the captured images. The time elapsed between the start of the test and the complete freezing of the water droplets was defined as the freezing time.

The coating was horizontally placed on a Peltier cooling plate. Next, a cylindrical mold with an inner diameter of 10 mm was placed on the surface of the coating. Finally, deionized water was injected into the mold. The temperature of the Peltier cooling plate was set to −10 °C and maintained for more than 40 min to ensure that the water inside the mold was completely frozen. The motion table was slowly moved to bring the force sensor into contact with the mold, and the mold from the coating surface was gradually removed [6]. The force sensor recorded the peak force in real time. The ice-adhesion strength was calculated on the basis of the value of the peak force and the area of the cylindrical mold. All the tests in this paper were repeated more than three times. The mean and the standard deviation of the data after multiple tests were calculated as the final results.

3. Results and Discussion

3.1. Morphology and Chemical Composition

The microstructures of coatings are shown in Figure 2. It can be seen that the coatings with different PTFE mass fractions have different microstructures. Without the addition of PTFE, the surface of the coating is smoother (Figure 2a,b). When the mass fraction of PTFE is 15.2%, a small amount of the lamellar structure appears on the surface of the coating. Thanks to the small amount of added PTFE, no obvious PTFE particles are found on the surface (Figure 2c,d). As the mass fraction of PTFE gradually increases, a rough structure is gradually formed on the surface. The surface of the coating with 34.9% mass fraction becomes uneven. A rough structure consisting of micron-size protrusions, pits and nano-size PTFE spherical particles is observed (Figure 2e,f). When the PTFE mass fraction is increased to 47.2%, the coating has the flattest rough structure, with nanoscale PTFE spherical particles all over the surface (Figure 2g,h). Notably, the surface of the coating with 58.8% mass fraction presents larger cracks and pores (yellow arrows). Many nanoscale PTFE spherical particles are embedded in the binder composed of epoxy and fluorosilicone resins (Figure 2i,j). This implies that there is a significant effect of PTFE mass fraction on the microstructure of the coating. When the PTFE mass fraction is too low, the PTFE particles are completely encapsulated by the binder on the surface, making it difficult to form a rough structure. When the PTFE mass fraction is too high, too many PTFE particles are beyond the binder's embedding range, and defects such as cracks and voids start to appear on the surface. Therefore, the most suitable PTFE mass fraction for one-step spraying is 47.2%, and the surface of the prepared coating has a uniform and flat rough structure.
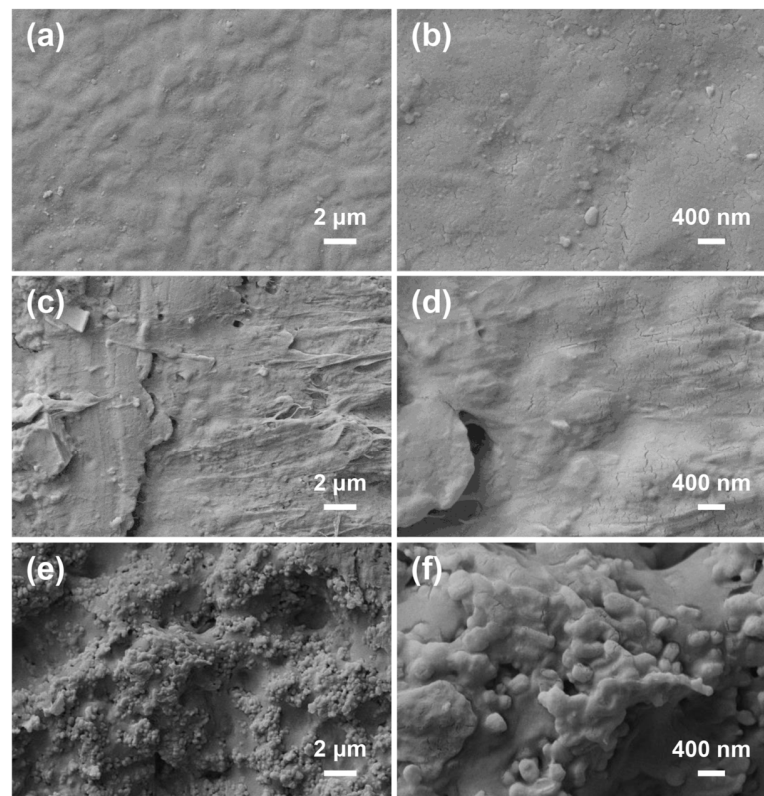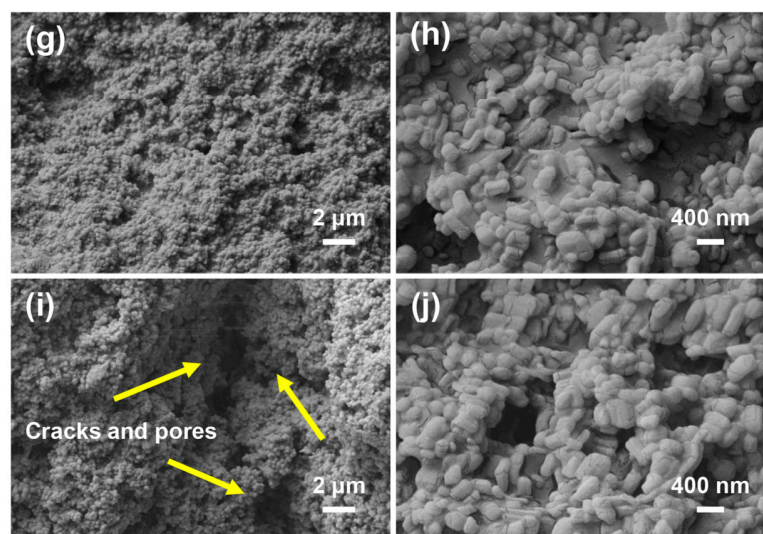

Figure 2. *Cont.*

Figure 2. Microstructures of coatings with different PTFE mass fractions: (**a**,**b**) 0%; (**c**,**d**) 15.2%; (**e**,**f**) 34.9%; (**g**,**h**) 47.2%; and (**i**,**j**) 58.8%.

In addition, the elemental distributions show that the surface of the coating is covered with F elements (Figure S1). This indicates that the fluorosilicone resin, FAS-17 and PTFE can be uniformly sprayed onto the surface of the coating, which is beneficial to the preparation of SHP coatings. The chemical compositions of the coatings are presented in Figure S2. The presence of a significant C–F bond on the surface of the SHP coating is detected. The addition of fluorosilicone resin and FAS-17 not only brings a large number of C–F bonds but also increases the adhesion of the coating. The rough structure of the coating is constructed of the C–F-bond-rich PTFE nanoparticles, which dramatically improves its hydrophobic properties.

3.2. Wettability

It is well known that the rough structure has a significant effect on the wetting performance of the coating [43,44]. The measurements for the apparent contact and sliding angles of the coatings are shown in Figure 3. Compared with the glass (40.5°), the apparent contact angles of the coatings are significantly increased (Figure 3a). The coatings with 0% and 15.2% mass fraction have similar apparent contact angles (113.4° and 115.9°, respectively). When the mass fraction of PTFE is 34.9%, the apparent contact angle of the coating increases to 154.1°. As the PTFE mass fraction further increases to 47.2% and 58.8%, the apparent contact angle of the coating increases to 164.7° and 165.7°, respectively. On the other hand, the sliding angle represents the rolling ability of the water droplets on the surface and is often used to evaluate the self-cleaning ability of the material [45]. The smaller the sliding angle, the stronger the rolling ability of the water droplet [46]. It can be seen from Figure 3b that the glass and coatings with lower mass fraction have a sliding angle higher than 90°. When the PTFE mass fraction is higher than 34.9%, the sliding angle of the coating starts to significantly decrease. The respective sliding angles of the coatings with 34.9%, 47.2% and 58.8% mass fractions decrease to 15.8°, 3.2° and 2.2°, respectively. A certain rough structure is formed on the surface of the coatings with the 34.9%, 47.2% and 58.8% mass fractions (Figure 2), which causes the coatings to have larger apparent contact angles. As the mass fraction of PTFE increases, the structure of the coating becomes more compact and the PTFE particles with low surface energy on the surface gradually increase. This results in a gradual decrease in the sliding angle of the coating. It can be found that the coatings with PTFE mass fractions of 47.2% and 58.8% achieve the standard of SHP materials. The water droplets can be held up by the air cushion in the rough structure of the SHP surface and exhibit a spherical shape [47].
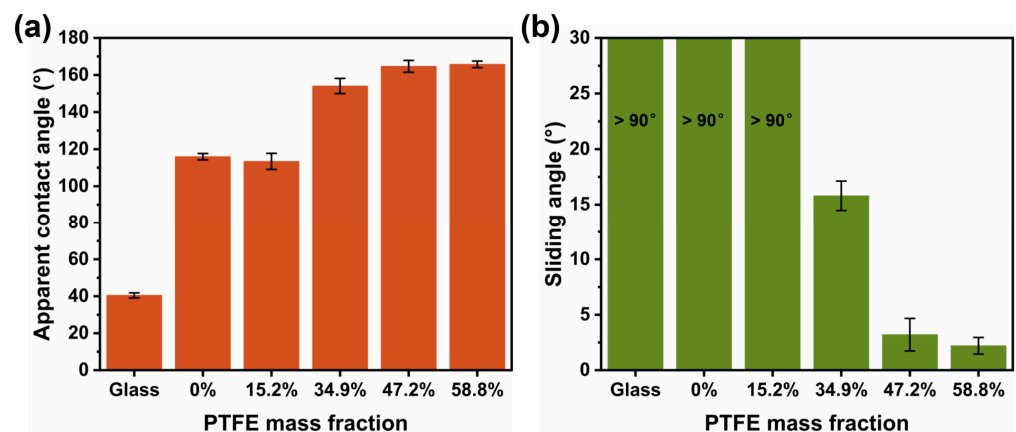
Figure 3. Apparent contact angle (**a**) and sliding angle (**b**) of water droplets placed on glass and coatings with different PTFE mass fractions.

To study the dynamic wetting performance of the coatings, water-droplet-bouncing tests at 25 °C were carried out. The results are displayed in Figures S3 and S4. It is clear that the water droplets on the surface of the coating with 47.2% mass fraction can rebound five times, while PTFE with mass fractions of 34.9% and 58.8% can rebound only three times. Moreover, the water-droplet-bouncing performance of the glass and coatings at −10 °C is shown in Figure S5. Notably, water droplets on the surface of the 47.2% mass fraction coating can still rebound once. This indicates that the 47.2% mass fraction coating has good water-droplet-bouncing performance in the ambient and low-temperature environments. The SHP coating can significantly decrease the possibility of water-droplet freezing by reducing the contact with water droplets.

The water-droplet-bouncing performance from coatings was quantitatively evaluated. The contact time and rebound height were measured for coatings with 34.9%, 47.2% and 58.8% mass fractions, as displayed in Figure 4. The time between the water droplet's impacting the surface and its leaving is defined as the contact time. A shorter contact time means a lower probability of water-droplet freezing [48]. The distance that the water droplet rebounds from the surface to the highest is defined as the rebound height. A higher rebound height indicates a lower energy loss of water droplets hitting the surface [49]. The rebound speed of the water droplets can be increased by the lower energy loss. This reduces the possibility of water droplets' being captured by the surface, which indirectly decreases the possibility of water droplets' freezing [50]. There is no bounce process for water droplets on the surface of the glass and the 0% and 15.2% mass fraction coatings. Therefore, the contact time is infinite, and the rebound height is 0 mm. The contact time of the three higher mass fraction coatings first decreases and then increases with increasing PTFE mass fraction. The coating with a 47.2% mass fraction has the smallest contact time (9.5 ms) (Figure 4a). However, the rebound heights of the three higher mass fraction coatings exhibit an opposite trend (first increasing and then decreasing). The rebound height of the 47.2% mass fraction coating is up to 4.58 mm (Figure 4b). On the other hand, the water-droplet-bouncing performance of the coating is degraded by the low-temperature environment. The contact time of the 34.9% and 58.8% mass fraction coatings increases to infinity, and the rebound height decreases to 0 mm. In contrast, the 47.2% mass fraction coating still has a contact time of 12.2 ms and a rebound height of 1.4 mm. This suggests that the 47.2% mass fraction coating has good water-droplet-bouncing performance in both room temperature and low-temperature environments.
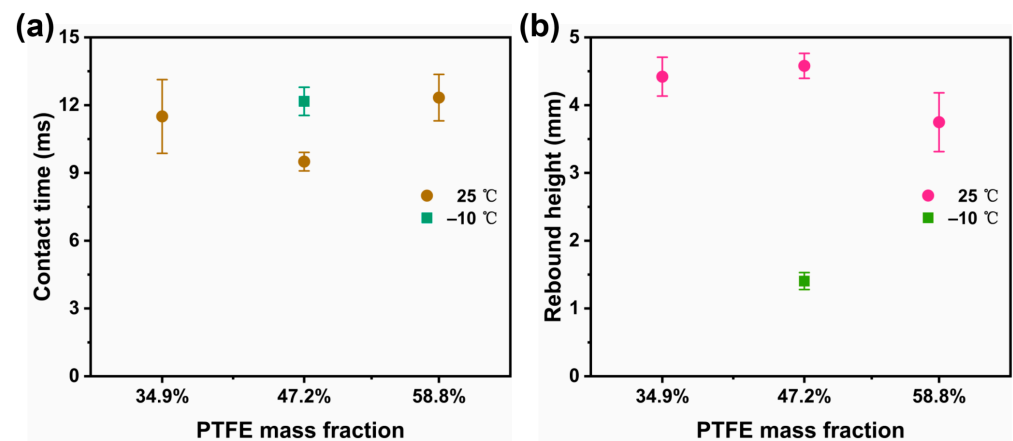
Figure 4. Contact time (**a**) and rebound height (**b**) of water droplets placed on coatings with 34.9%, 47.2% and 58.8% mass fractions.

The glass and the coatings with different mass fractions show different water-droplet-bouncing behaviors in 25 and −10 °C environments. The main reason for this is the difference in the microstructure of the surfaces. The surfaces of the glass and the 0% and 15.2% mass fraction coatings are smoother, and no rough structure is formed (Figure 2). Hence, the surfaces have greater water-droplet-adhesion values. This causes the water droplets that impact the surface to easily spread on the surface, consuming the energy of the impacting water droplets and making it difficult for them to bounce off. For the coatings with 34.9%, 47.2% and 58.8% mass fraction, a certain rough structure (Figure 2) with good hydrophobicity (Figure 3) is observed on the surface. The energy loss is effectively reduced by the air cushion and the low-surface-energy PTFE particles. Thus, the water droplets that impact the surface can be adequately rebounded. The coating with 47.2% mass fraction has the most uniform rough structure. This results in the highest number of rebounds, the smallest contact time and the largest rebound height (Figure 4). In the low-temperature environment, the 34.9% and 58.8% mass fraction coatings basically fail, and the water droplets on the surface have difficulty bouncing, while the 47.2% mass fraction coating still exhibits better water-droplet-bouncing performance.

3.3. Anti-icing Properties

The anti-frosting performance values of the glass and coatings are shown in Figure 5. It can be seen that the glass is completely frosted in 499 s. This is due to the presence of many hydrophilic groups on the smooth glass, and they easily adsorb the water vapor to form a water film and frost. The anti-frosting performance of the 0% and 15.2% mass fraction coatings is improved by the low-surface-energy substances on the surface, with complete frosting times of around 679 and 590 s, respectively. When the mass fraction increases to 34.9%, the complete frosting time is prolonged to 820 s thanks to the rough structure of the coating (Figure 2e). With a further increase in mass fraction to 47.2%, the surface of the coating has a more uniform rough structure (Figure 2g). The excellent water-repellent and self-cleaning properties make it difficult for water vapor to gather into water beads on the surface. As a result, the complete frosting time is significantly extended to 1499 s. For the 58.8% mass fraction coating, there are few defects in the rough structure of the surface (Figure 2i), which reduces the complete frosting time to 1312 s.
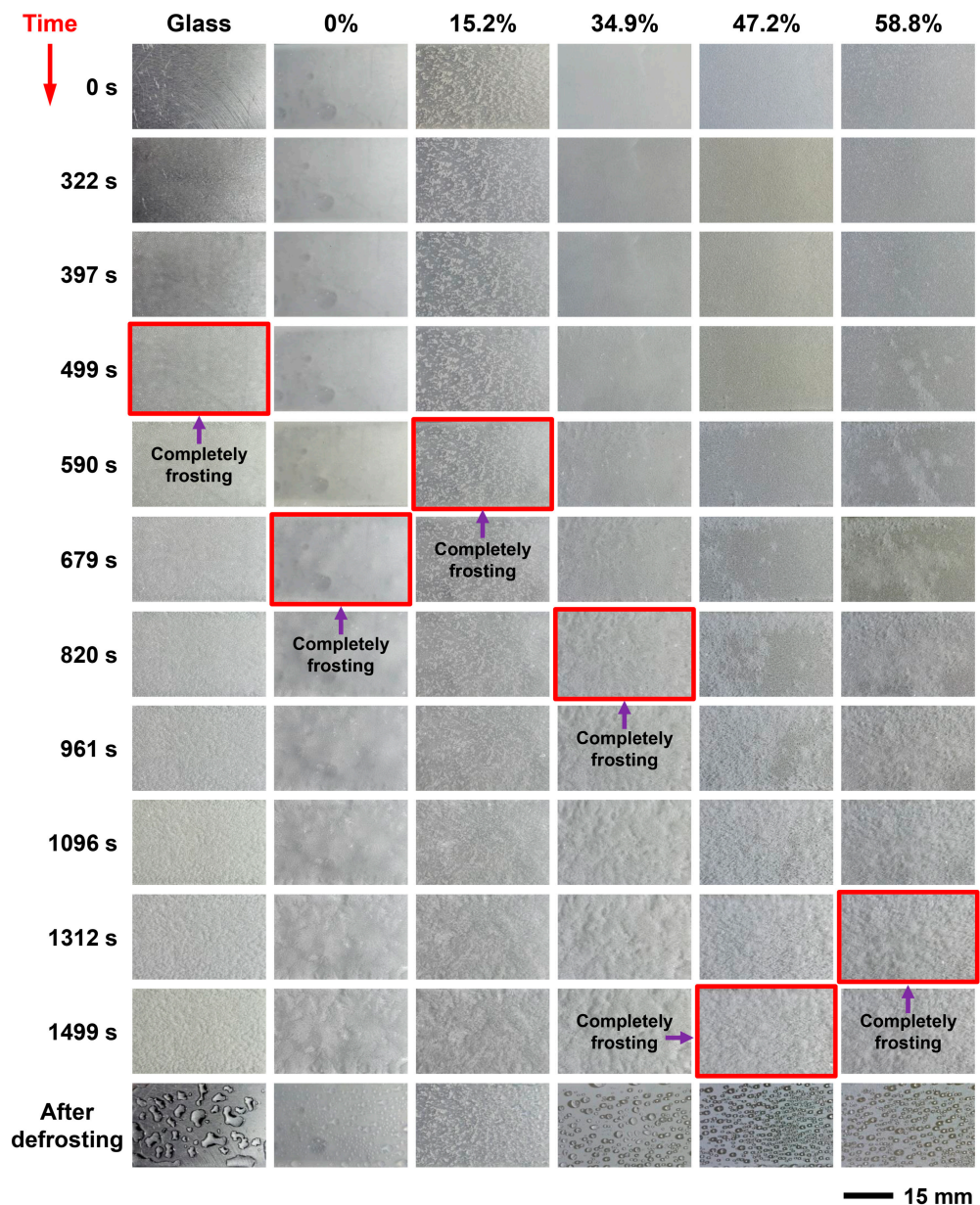
Figure 5. Anti-frosting performance of glass and coatings with different mass fractions.

The complete frosting time of the 47.2% mass fraction coating is three times longer than that of the glass. This demonstrates that the prepared SHP coatings have good anti-frosting properties and can effectively retard frosting. After the frost has completely melted, a large area of water film appears on the surface of the glass. Larger water droplets are distributed on the surface of the coatings with 0% and 15.2% mass fractions, while 34.9% and 58.8% mass fraction coatings have smaller water droplets all over the surface. In particular, the size of the water droplets distributed on the surface of the 47.2% mass fraction coating is much smaller. This suggests that the 47.2% mass fraction coating has good water-repellent properties after defrosting.

The water-droplet-freezing tests were carried out on the glass and coatings. The freezing process of water droplets is presented in Figure 6. In general, the water droplets on the surface are slowly cooled and frozen by heat transfer [51]. The transparent water droplets are gradually frozen during a slow heterogeneous nucleation process, eventually transforming into an opaque frozen state. The freezing times of the water droplets on the surface of the glass and coatings are displayed in Figure 7. Similar to the wetting

performance (Figure 3), the glass has the shortest freezing time (259.3 s). The freezing times of the 0% and 15.2% mass fraction coatings are improved, extending to 617.5 and 542.8 s, respectively. When the mass fraction is increased to 34.9%, the freezing time of the coating is prolonged to 814.8 s. It is found that the SHP coating prepared with 47.2% mass fraction exhibits the highest freezing time (1295.3 s), which is about five times higher than that of the glass. This is because the 47.2% mass fraction coating has a uniform rough structure, and the water droplets on the surface show a Cassie state (Figure 2g). At this time, the actual contact area of the water droplets with a rough structure is smaller. The heat-transfer efficiency is greatly reduced by the air cushion in the structure, effectively retarding the freezing of the water droplets [15,52]. Furthermore, the freezing time of the 58.8% mass fraction coating is slightly decreased, to 1033.3 s. This is attributed to the formation of partial defects in the rough structure that had been caused by the addition of excess PTFE particles (Figure 2i).
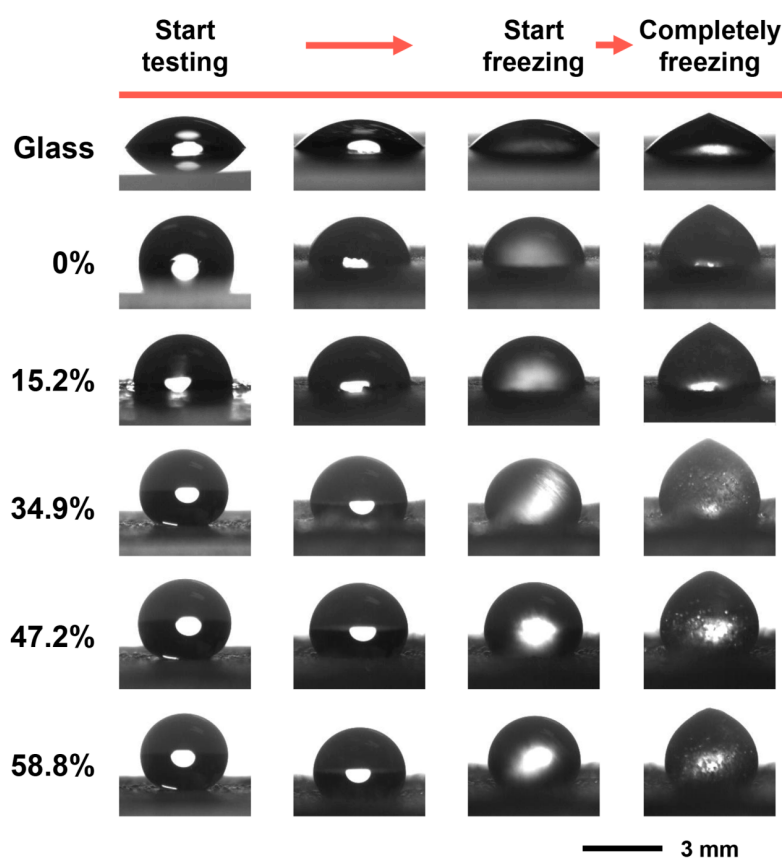
Figure 6. Freezing process of water droplets placed on glass and coatings with different PTFE mass fractions.

In the low-temperature and high-humidity environment, the rough structure is easily invaded by water vapor and frosted, resulting in the failure of the SHP surface used for anti-icing [40,53]. From Figures 5 and 7, it can be found that frosting and icing can be significantly retarded by the prepared SHP coatings. However, frosting and icing will still eventually occur with time. Therefore, the SHP coatings for anti-icing should not only be useful in delaying icing but also have good icephobic properties that facilitate effective deicing after icing [54]. The ice-adhesion strengths of the glass and coatings were measured before and after frosting, as shown in Figure 8. Compared with the highest ice-adhesion strength of glass (260.4 kPa), the ice-adhesion strength of the prepared coatings is significantly lower. The coating without PTFE particles has higher ice-adhesion strength (118.6 kPa). The ice-adhesion strength of the 15.2% mass fraction coating decreases to 82.6 kPa, which reaches the standard of icephobic materials (below 100 kPa) [55]. The

ice-adhesion strength of the coating first decreases and then increases as the mass fraction continues to increase, which is the opposite of the changing trend of freezing time (Figure 7). The ice-adhesion strengths of the coatings with 34.9%, 47.2% and 58.8% mass fraction are 76.7, 39.8 and 62.4 kPa, respectively. This indicates that the SHP coatings prepared with 47.2% mass fraction can actively deice under the action of external forces (gravity or wind). It is beneficial to the effective deicing of insulators after icing. In addition, the ice-adhesion strength of the glass and coatings changes less after frosting. The variation trend of ice adhesion strength for glass and coatings is consistent before and after frosting. After frosting, the 47.2% mass fraction coating still has the lowest ice adhesion strength (47.2 kPa).
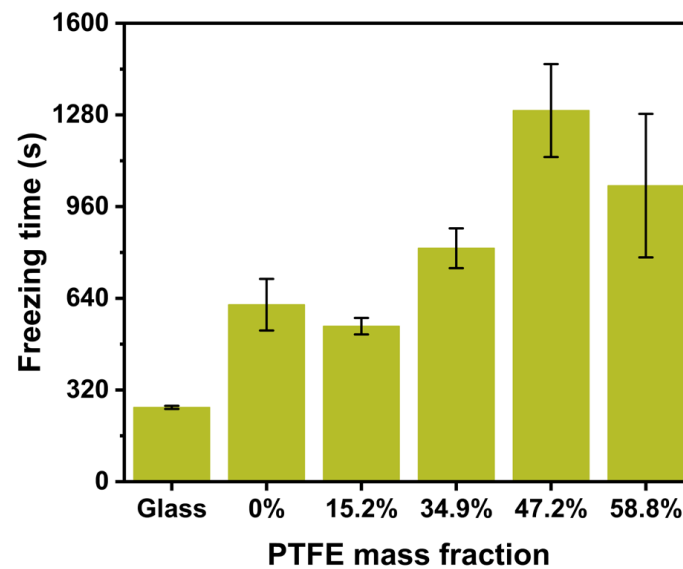

Figure 7. Freezing time of water droplets placed on glass and coatings with different PTFE mass fractions.
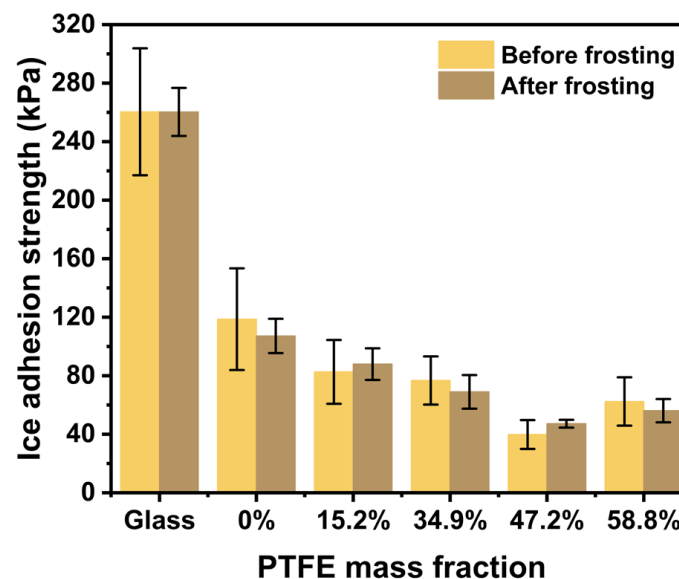

Figure 8. Ice-adhesion strength of water droplets placed on glass and coatings with different PTFE mass fractions.

3.4. Anti-Icing Durability

To evaluate the anti-icing durability performance of SHP coatings, icing–deicing cycle tests were performed on 47.2% mass fraction coatings. The apparent contact and sliding

angles after icing–deicing cycles were measured, and the results are displayed in Figure 9a. As the number of icing–deicing cycles increases, the apparent contact angle of the coating slowly decreases, while its sliding angle rapidly increases. After 20 cycles, the apparent contact angle of the coating decreases to 149.1°, and the sliding angle increases to 21.3°. This indicates that the icing–deicing cycle has a significant effect on the wetting performance of the SHP coating. The hydrophobicity and self-cleaning properties of the coating are degraded after the icing–deicing cycle. In addition, the ice-adhesion strength after icing–deicing cycles is presented in Figure 9b. Similar to the variation trend for the sliding angle (Figure 9a), the ice-adhesion strength of the coating gradually increases with the number of icing–deicing cycles. The ice-adhesion strength of the coating increases to 90.4 kPa after 20 icing–deicing cycles. It can be expected that the hydrophobicity, anti-icing and icephobic properties of the coating will gradually degrade as the number of icing–deicing cycles continues to increase [56].
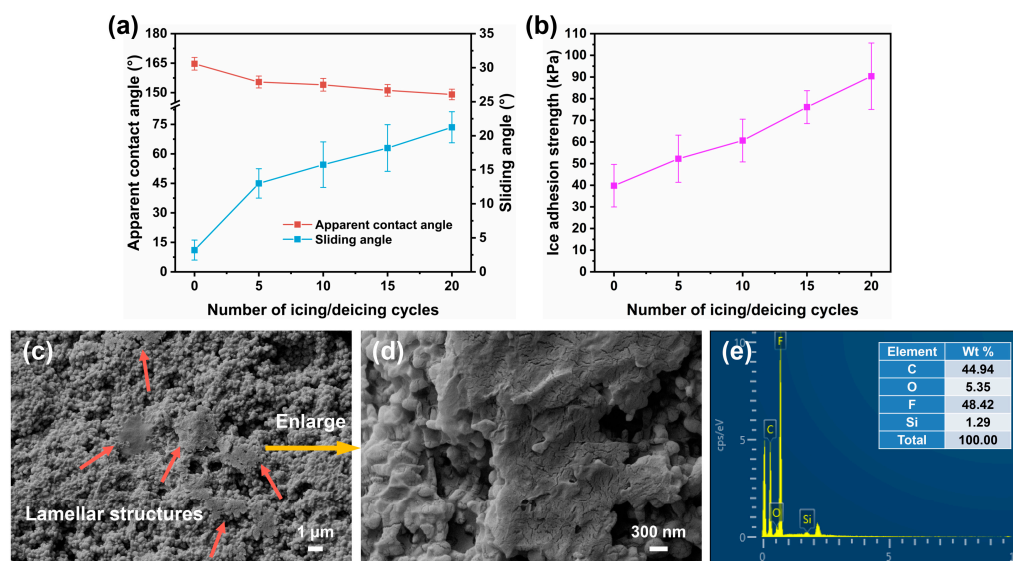
Figure 9. Wettability (**a**), ice-adhesion strength (**b**), micromorphology (**c**,**d**) and EDS spectrum (**e**) of 47.2% mass fraction coating after icing–deicing cycles.

The microstructure and elemental composition of the 47.2% mass fraction coating after icing–deicing cycles are shown in Figure 9c–e. Unlike the microstructure before icing–deicing cycles (Figure 2g), more large lamellar structures (red arrows) are observed on the surface after 20 icing–deicing cycles (Figure 9c,d). The surface of the coating has the same elemental species before and after the icing–deicing cycles (Figure 9e). According to Figure S1, it can be found that the content of the F element decreases after the icing–deicing cycles. This is attributed to the loss of low-surface-energy groups on the surface. On the other hand, during the icing process, the water film on the surface undergoes heterogeneous nucleation and gradually ices from the bottom to the top. At this time, a small amount of water is present embedded in the rough structure and frozen together. For the ice-adhesion-strength test, horizontal thrusts were used to push frozen icicles away from the surface. This causes the ice embedded in the rough structure and the coating to be forcibly pushed off. Thus, a complex force action between the ice and the rough structure is created.

It is known that PTFE is a polymer with lower hardness compared to nanoparticles such as SiO_2. This contributes to the poor mechanical properties of PTFE particles. The surface-bonded PTFE particles encounter difficulty in resisting the destruction of cyclic icing–deicing, which gradually damages the rough structure (Figure 9c,d). It has been suggested that the rough structure of the SHP coating is easily damaged by machinery and that the low-surface-energy substances are prone to be lost during the service process [57,58]. This will lead to the premature failure of SHP coatings. Therefore, after the

icing–deicing cycle tests, the disruption of the rough structure and the loss of low-surface-energy substances contribute to a decrease in the water-repellent properties (Figure 9a) and an increase in ice-adhesion strength (Figure 9b). Agreeing with the results of the present work, Kulinich et al. [59,60] found that the significant interfacial stresses induced by water expansion during the icing–deicing process lead to a disruption of the rough structure, causing an increase in the ice-adhesion strength. Using cryoscanning electron microscopy, it was observed that the tips of the superhydrophobic structures were embedded in the frozen water, resulting in localized damage to the rough structure after deicing [61].

3.5. Anti-Icing Mechanism

Combined with the above results, the schematic diagram of the anti-frosting, anti-icing and icephobic mechanisms of the SHP coating prepared with 47.2% mass fraction was constructed, as depicted in Figure 10. The black arrow indicates the heat transfer process, the light red arrow denotes the movement direction of the water vapor, and the dark red arrow represents the air cushion. It is well known that the surface of glass is very smooth and flat. The surface of glass is distributed with many hydrophilic groups, and water droplets tend to adhere to the surface. This means that glass in a low-temperature and high-humidity environment is highly susceptible to adsorbing water vapor and forming a water film. The nucleation and growth of frost crystals on the surface are significantly promoted by the presence of water film [62,63]. Therefore, at higher heat-transfer rates, the glass is completely frosted after 499 s of frosting tests (Figure 5). In contrast, the surface of the prepared SHP coating has a uniform rough structure (Figure 2g). The air cushion in the structure and the water-repellent PTFE particles make it difficult for water vapor to form aggregated water droplets. This effectively retards the formation of condensation film and frosting on the surface [64,65]. On the other hand, the epoxy/fluorosilicone/PTFE coating covering the surface resembles a layer of heat-transfer resistance, which also to some extent reduces the heat-transfer rate [66]. As a result, the complete frosting time of the SHP coating is extended to 1499 s (Figures 5 and 10a).
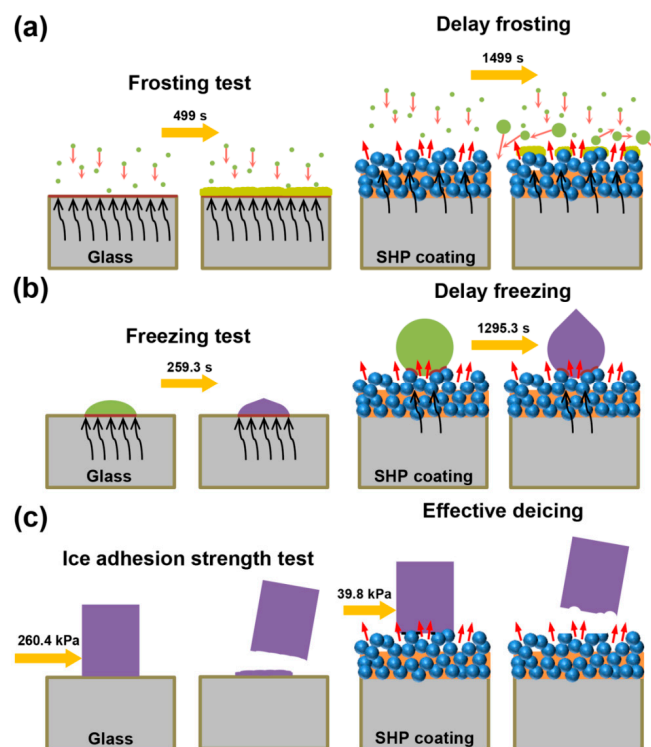
Figure 10. Schematic diagram of anti-frosting (**a**), anti-icing (**b**) and icephobic (**c**) mechanisms of SHP coating.

A low apparent contact angle (40.5°) and a large sliding angle were measured on the surface of the glass (Figure 3). The water droplets spread out on the surface, significantly increasing the contact area between the water droplets and the surface of the glass. Thus, the faster heat-transfer rate causes the water droplets on the glass to completely freeze in 259.3 s. Furthermore, a uniform rough structure (Figure 2g) with good water-repellent properties (Figures 4 and S3–S5) is prepared on the surface. It has been indicated that there are many air cushions in the rough structure, which can effectively decrease the contact area between water droplets and the SHP coating [2,43]. The intrinsic contact angle of the SHP coating is taken to be 115.9°. According to the classical Cassie model [67,68], the solid–liquid contact area fraction of the SHP coating is calculated to be only 6.31%. This implies that the prepared SHP coating has a large gas–liquid contact area with water droplets. Hence, water droplets on the surface have a high center of gravity and show a spherical shape that can easily roll off the surface. This prevents the surface from being wetted, further reducing the possibility of icing. On the other hand, it is known that air is a poor conductor of heat. The heat-transfer rate can be effectively decreased by the large area of air cushion in the rough structure, and the freezing of water droplets is greatly retarded [69]. These cause the delayed freezing time of the SHP coating to be as long as 1295.3 s (Figures 7 and 10b).

The hydrophilic group causes the deionized water to be completely adsorbed on the surface of the glass. Under the effect of hydrophilic hydrogen bonding [70], a huge adhesion force is formed after freezing. This results in an ice-adhesion strength of up to 260.4 kPa measured for glass. It has been reported that the main factors affecting the ice-adhesion force are hydrogen bonding, van der Waals forces and a direct electrostatic interaction. Low-surface-energy materials can decrease ice-adhesion forces by reducing electrostatic interactions [71] and shielding van der Waals forces [72]. The surface of the SHP coating prepared in this work has a large number of low-surface-energy PTFE particles (Figures 2g and S1). This can effectively mitigate the influence of electrostatic and van der Waals forces on ice-adhesion strength. On the other hand, the smaller the contact area between the ice and the solid surface, the lower the ice-adhesion strength [73,74]. The solid–liquid contact area is remarkably decreased by the rough structure (Figures 2 and 3). It can be inferred that the surface of the SHP coating has a small solid-ice contact area, which can significantly reduce the ice-adhesion strength. Notably, a large amount of air is trapped by the rough structure of the SHP coating. The air cushions formed in the structure can act as microcracks and stress-concentration points. This will accelerate the crack extension and thus reduce the ice-adhesion strength [71,75]. In addition, when measuring the ice-adhesion strength, the air in the rough structure is squeezed by the ice and the mold. In this case, the pressure inside the air cushion is increased, causing the air to push back against the ice on the surface, thereby decreasing the ice-adhesion strength [62]. Therefore, the ice-adhesion strength of the SHP coating is significantly reduced, to 39.8 kPa (Figures 8 and 10c).

4. Conclusions

The relationships between the microstructure, chemical composition, wettability, anti-frosting, anti-icing and icephobic properties of the epoxy/fluorosilicone/PTFE coatings prepared by one-step spraying were investigated. There was a significant effect of the PTFE mass fraction on the wetting, anti-frosting, anti-icing and icephobic properties of the coatings. Compared with glass and other mass fraction coatings, the SHP coating prepared with 47.2% mass fraction had good water-repellent properties (an apparent contact angle of 164.7°, a sliding angle of 3.2°, water-droplet bounce times of five, a contact time of 9.5 ms and a rebound height of 4.58 mm). In the low-temperature environment, the SHP coating exhibited excellent anti-frosting (a delayed frosting time of 1499 s), anti-icing (a delayed freezing time of 1295.3 s) and icephobic (an ice-adhesion strength of 39.8 kPa) properties, which were attributed to the uniform rough structure and low-surface-energy substances. After 20 icing–deicing cycle tests, the rough structure was partially destroyed, and a small

number of the hydrophobic groups on the surface were lost. This resulted in a degradation of the hydrophobic and icephobic properties of the SHP coating.

Further research is needed to improve the anti-icing durability of SHP coatings. It is noteworthy that the prepared SHP coating showed outstanding anti-frosting, anti-icing and icephobic properties compared with glass. This can provide a reference for the preparation of anti-icing coatings based on glass insulators, and the possibility of applying SHP coatings in practical power engineering is increased.

Supplementary Materials: The following supporting information can be downloaded at https://www.mdpi.com/article/10.3390/coatings13030569/s1, Figure S1: EDS spectra of coatings with different PTFE mass fractions; Figure S2: FTIR spectra of coatings with 0% and 47.2% mass fraction; Figure S3: Water-droplet-bouncing performance values of glass and of the 0%, 15.2% and 34.9% mass fraction coatings at 25 °C; Figure S4: Water-droplet-bouncing performance values of coatings with 47.2% and 58.8% mass fraction at 25 °C; Figure S5: Water-droplet-bouncing performance values of glass and coatings with different mass fractions at −10 °C [76–85].

Institutional Review Board Statement: Not applicable.

Informed Consent Statement: Not applicable.

Data Availability Statement: The raw/processed data required to reproduce these findings cannot be shared at this time, for legal or ethical reasons.

Conflicts of Interest: The authors declare no conflict of interest.

References

1. Hu, Q.; Yang, H.; Jiang, X.; Shu, L.; Yang, X. Investigation on one-step preparation and anti-icing experiments of robust super-hydrophobic surface on wind turbine blades. *Cold Reg. Sci. Technol.* **2022**, *195*, 103484. [CrossRef]
2. Qi, Y.; Yang, Z.; Chen, T.; Xi, Y.; Zhang, J. Fabrication of superhydrophobic surface with desirable anti-icing performance based on micro/nano-structures and organosilane groups. *Appl. Surf. Sci.* **2020**, *501*, 144165. [CrossRef]
3. Shu, L.C.; Wang, S.J.; Jiang, X.L.; Hu, Q.; Yang, X.Y.; Yang, S.; Chen, J. Effect of Grading Ring on Ice Characteristics and Flashover Performance of 220 kV Composite Insulators with Different Shed Configurations. *IEEE Trans. Dielectr. Electr. Insul.* **2015**, *22*, 951–960. [CrossRef]
4. Olad, A.; Maryami, F.; Mirmohseni, A.; Shayegani-Akmal, A.A. Potential of slippery liquid infused porous surface coatings as flashover inhibitors on porcelain insulators in icing, contaminated, and harsh environments. *Prog. Org. Coatings* **2020**, *151*, 106082. [CrossRef]
5. Sarma, J.; Zhang, L.; Guo, Z.; Dai, X. Sustainable icephobicity on durable quasi-liquid surface. *Chem. Eng. J.* **2021**, *431*, 133475. [CrossRef]
6. Yuan, Y.; Xiang, H.; Liu, G.; Liao, R. Fabrication of phase change microcapsules and their applications to anti-icing coating. *Surfaces Interfaces* **2021**, *27*, 101516. [CrossRef]
7. Jiang, X.; Fan, C.; Xie, Y. New method of preventing ice disaster in power grid using expanded conductors in heavy icing area. *IET Gener. Transm. Distrib.* **2019**, *13*, 536–542. [CrossRef]
8. Zhou, A.; Zhang, Y.; Qu, Q.; Li, F.; Lu, T.; Liu, K.; Huang, C. Well-defined multifunctional superhydrophobic green nanofiber membrane based-polyurethane with inherent antifouling, antiadhesive and photothermal bactericidal properties and its application in bacteria, living cells and zebra fish. *Compos. Commun.* **2021**, *26*, 100758. [CrossRef]
9. Zhang, X.; Wang, R.; Long, F.; Zhou, T.; Hu, W.; Liu, L. Durable superhydrophobic coating derived from hard-soft technology with enhanced anticorrosion performance. *Corros. Sci.* **2021**, *193*, 109889. [CrossRef]
10. Wang, X.; Ding, H.; Wang, C.H.; Zhou, R.; Li, Y.Z.; Li, W.; Ao, W.H. Self-healing superhydrophobic A-SiO2/N-TiO2@HDTMS coating with self-cleaning property. *Appl. Surf. Sci.* **2021**, *567*, 150808. [CrossRef]
11. Pakdel, E.; Wang, J.; Varley, R.; Wang, X. Recycled carbon fiber nonwoven functionalized with fluorine-free superhydrophobic PDMS/ZIF-8 coating for efficient oil-water separation. *J. Environ. Chem. Eng.* **2021**, *9*, 106329. [CrossRef]

12. Cao, L.; Jones, A.K.; Sikka, V.K.; Wu, J.; Gao, D. Anti-Icing Superhydrophobic Coatings. *Langmuir* **2009**, *25*, 12444–12448. [CrossRef] [PubMed]

13. Guo, P.; Zheng, Y.; Wen, M.; Song, C.; Lin, Y.; Jiang, L. Icephobic/Anti-Icing Properties of Micro/Nanostructured Surfaces. *Adv. Mater.* **2012**, *24*, 2642–2648. [CrossRef]

14. Guo, H.; Xing, Y.; Yuan, H.; Zhang, R.; Zhang, Y.; Deng, P. Improving the anti-icing performance of superhydrophobic surfaces by nucleation inhibitor. *Surf. Eng.* **2019**, *36*, 621–627. [CrossRef]

15. Jiang, G.; Chen, L.; Zhang, S.; Huang, H.-X. Superhydrophobic SiC/CNTs Coatings with Photothermal Deicing and Passive Anti-Icing Properties. *ACS Appl. Mater. Interfaces* **2018**, *10*, 36505–36511. [CrossRef] [PubMed]

16. Nosonovsky, M.; Hejazi, V. Why Superhydrophobic Surfaces Are Not Always Icephobic. *ACS Nano* **2012**, *6*, 8488–8491. [CrossRef]

17. Starostin, A.; Strelnikov, V.; Valtsifer, V.; Lebedeva, I.; Legchenkova, I.; Bormashenko, E. Robust icephobic coating based on the spiky fluorinated Al2O3 particles. *Sci. Rep.* **2021**, *11*, 5394. [CrossRef] [PubMed]

18. Xiang, H.; Yuan, Y.; Zhang, C.; Dai, X.; Zhu, T.; Song, L.; Gai, Y.; Liao, R. Key Factors Affecting Durable Anti-Icing of Slippery Surfaces: Pore Size and Porosity. *ACS Appl. Mater. Interfaces* **2022**, *15*, 3599–3612. [CrossRef]

19. Yuan, Y.; Xiang, H.; Liu, G.; Wang, L.; Liu, H.; Liao, R. Self-Repairing Performance of Slippery Liquid Infused Porous Surfaces for Durable Anti-Icing. *Adv. Mater. Interfaces* **2022**, *9*, 202101968. [CrossRef]

20. Liu, G.Y.; Yuan, Y.; Zhou, J.; Jiang, Y.D.; Wang, L. Anti-frosting/anti-icing property of nano-ZnO superhydrophobic surface on Al alloy prepared by radio frequency magnetron sputtering. *Mater. Res. Express* **2020**, *7*, 026401. [CrossRef]

21. Zuo, Z.; Song, X.; Liao, R.; Zhao, X.; Yuan, Y. Understanding the anti-icing property of nanostructured superhydrophobic aluminum surface during glaze ice accretion. *Int. J. Heat Mass Transf.* **2018**, *133*, 119–128. [CrossRef]

22. Patil, D.; Aravindan, S.; Sarathi, R.; Rao, P.V. Fabrication of self-cleaning superhydrophobic silicone rubber insulator through laser texturing. *Surf. Eng.* **2020**, *37*, 308–317. [CrossRef]

23. Wang, Y.; Zhao, W.; Han, L.; Tam, K.C. Superhydrophobic surfaces from sustainable colloidal systems. *Curr. Opin. Colloid Interface Sci.* **2021**, *57*, 101534. [CrossRef]

24. Han, T.; Kim, J.H.; Kim, Y.D.; Ahn, D.J.; Lim, D.-K. Solution-Based One-Step Preparation of Three-Dimensional Self-Assembled Octadecyl Silica Nanosquare Plate and Microlamella Structures for Superhydrophobic and Icephobic Surfaces. *Langmuir* **2021**, *37*, 5886–5894. [CrossRef]

25. Pan, R.; Zhang, H.; Zhong, M. Triple-Scale Superhydrophobic Surface with Excellent Anti-Icing and Icephobic Performance via Ultrafast Laser Hybrid Fabrication. *ACS Appl. Mater. Interfaces* **2020**, *13*, 1743–1753. [CrossRef] [PubMed]

26. Sun, R.; Zhao, J.; Li, Z.; Qin, N.; Mo, J.; Pan, Y.; Luo, D. Robust superhydrophobic aluminum alloy surfaces with anti-icing ability, thermostability, and mechanical durability. *Prog. Org. Coat.* **2020**, *147*, 105745. [CrossRef]

27. Liao, R.; Zuo, Z.; Guo, C.; Zhuang, A.; Zhao, X.; Yuan, Y. Anti-icing performance in glaze ice of nanostructured film prepared by RF magnetron sputtering. *Appl. Surf. Sci.* **2015**, *356*, 539–545. [CrossRef]

28. Liao, R.; Zuo, Z.; Guo, C.; Zhuang, A.; Yuan, Y.; Zhao, X.; Zhang, Y. Ice accretion on superhydrophobic insulators under freezing condition. *Cold Reg. Sci. Technol.* **2015**, *112*, 87–94. [CrossRef]

29. Qin, C.; Mulroney, A.T.; Gupta, M.C. Anti-icing epoxy resin surface modified by spray coating of PTFE Teflon particles for wind turbine blades. *Mater. Today Commun.* **2020**, *22*, 100770. [CrossRef]

30. Lei, S.; Wang, F.; Fang, X.; Ou, J.; Li, W. Icing behavior of water droplets impinging on cold superhydrophobic surface. *Surf. Coat. Technol.* **2019**, *363*, 362–368. [CrossRef]

31. Pan, S.; Wang, N.; Xiong, D.; Deng, Y.; Shi, Y. Fabrication of superhydrophobic coating via spraying method and its applications in anti-icing and anti-corrosion. *Appl. Surf. Sci.* **2016**, *389*, 547–553. [CrossRef]

32. Zhang, F.; Qian, H.; Wang, L.; Wang, Z.; Du, C.; Li, X.; Zhang, D. Superhydrophobic carbon nanotubes/epoxy nanocomposite coating by facile one-step spraying. *Surf. Coat. Technol.* **2018**, *341*, 15–23. [CrossRef]

33. Pan, L.; Xue, P.; Wang, M.; Wang, F.; Guo, H.; Yuan, X.; Zhong, L.; Yu, J. Novel superhydrophobic carbon fiber/epoxy composites with anti-icing properties. *J. Mater. Res.* **2021**, *36*, 1695–1704. [CrossRef]

34. Chen, H.; Wang, F.; Fan, H.; Hong, R.; Li, W. Construction of MOF-based superhydrophobic composite coating with excellent abrasion resistance and durability for self-cleaning, corrosion resistance, anti-icing, and loading-increasing research. *Chem. Eng. J.* **2021**, *408*, 127343. [CrossRef]

35. Daneshmand, H.; Sazgar, A.; Araghchi, M. Fabrication of robust and versatile superhydrophobic coating by two-step spray method: An experimental and molecular dynamics simulation study. *Appl. Surf. Sci.* **2021**, *567*, 150825. [CrossRef]

36. Zhang, F.; Zhao, J.; Wang, L.; Guan, Z. Experimental Investigation on Outdoor Insulation for DC Transmission Line at High Altitudes. *IEEE Trans. Power Deliv.* **2009**, *25*, 351–357. [CrossRef]

37. Jiang, X.; Xiang, Z.; Zhang, Z.; Hu, J.; Hu, Q.; Shu, L. Comparison on ac icing flashover performance of porcelain, glass, and composite insulators. *Cold Reg. Sci. Technol.* **2014**, *100*, 1–7. [CrossRef]

38. Arianpour, F.; Farzaneh, M.; Kulinich, S. Hydrophobic and ice-retarding properties of doped silicone rubber coatings. *Appl. Surf. Sci.* **2013**, *265*, 546–552. [CrossRef]

39. Jiang, X.; Wang, S.; Zhang, Z.; Xie, S.; Wang, Y. Study on AC Flashover Performance and Discharge Process of Polluted and Iced IEC Standard Suspension Insulator String. *IEEE Trans. Power Deliv.* **2006**, *22*, 472–480. [CrossRef]

40. Varanasi, K.K.; Deng, T.; Smith, J.D.; Hsu, M.; Bhate, N. Frost formation and ice adhesion on superhydrophobic surfaces. *Appl. Phys. Lett.* **2010**, *97*, 234102. [CrossRef]

41. Hao, Q.; Pang, Y.; Zhao, Y.; Zhang, J.; Feng, J.; Yao, S. Mechanism of Delayed Frost Growth on Superhydrophobic Surfaces with Jumping Condensates: More Than Interdrop Freezing. *Langmuir* **2014**, *30*, 15416–15422. [CrossRef] [PubMed]

42. Chen, X.; Ma, R.; Zhou, H.; Zhou, X.; Che, L.; Yao, S.; Wang, Z. Activating the Microscale Edge Effect in a Hierarchical Surface for Frosting Suppression and Defrosting Promotion. *Sci. Rep.* **2013**, *3*, srep02515. [CrossRef] [PubMed]

43. Siddiqui, A.R.; Li, W.; Wang, F.; Ou, J.; Amirfazli, A. One-step fabrication of transparent superhydrophobic surface. *Appl. Surf. Sci.* **2020**, *542*, 148534. [CrossRef]

44. Chen, L.; Nie, Q.; Hu, T.; Bennett, P.; Zheng, Z.; Yang, Q.; Liu, D. Hydrophobic recovery of femtosecond laser processed silicone rubber insulator surfaces. *J. Appl. Polym. Sci.* **2021**, *138*, 50835. [CrossRef]

45. Wu, Y.-L.; Zheng, J.-W.; Muneeshwaran, M.; Yang, K.-S.; Wang, C.-C. Moist air condensation heat transfer enhancement via superhydrophobicity. *Int. J. Heat Mass Transf.* **2021**, *182*, 121973. [CrossRef]

46. Hu, J.; Jiang, G. Superhydrophobic coatings on iodine doped substrate with photothermal deicing and passive anti-icing properties. *Surf. Coatings Technol.* **2020**, *402*, 126342. [CrossRef]

47. Wang, G.; Zhou, J.; Wang, M.; Zhang, Y.; Zhang, Y.; He, Q. A superhydrophobic surface with aging resistance, excellent mechanical restorablity and droplet bounce properties. *Soft. Matter.* **2020**, *16*, 5514–5524. [CrossRef]

48. Wang, H.; Wu, Q.; Okagaki, J.; Alizadeh, A.; Shamim, J.A.; Hsu, W.-L.; Daiguji, H. Bouncing behavior of a water droplet on a super-hydrophobic surface near freezing temperatures. *Int. J. Heat Mass Transf.* **2021**, *174*, 121304. [CrossRef]

49. Chu, Z.; Jiao, W.; Huang, Y.; Yan, M.; Zheng, Y.; Wang, R.; He, X. Smart Superhydrophobic Films with Self-Sensing and Anti-Icing Properties Based on Silica Nanoparticles and Graphene. *Adv. Mater. Interfaces* **2020**, *7*, 2000492. [CrossRef]

50. Jung, S.; Dorrestijn, M.; Raps, D.; Das, A.; Megaridis, C.M.; Poulikakos, D. Are Superhydrophobic Surfaces Best for Icephobicity? *Langmuir* **2011**, *27*, 3059–3066. [CrossRef]

51. Zheng, M.; Guo, Z.; Dong, W.; Guo, X. Experimental investigation on ice accretion on a rotating aero-engine spinner with hydrophobic coating. *Int. J. Heat Mass Transf.* **2019**, *136*, 404–414. [CrossRef]

52. Li, X.; Wang, G.; Moita, A.S.; Zhang, C.; Wang, S.; Liu, Y. Fabrication of bio-inspired non-fluorinated superhydrophobic surfaces with anti-icing property and its wettability transformation analysis. *Appl. Surf. Sci.* **2020**, *505*, 144386. [CrossRef]

53. Wier, K.A.; McCarthy, T.J. Condensation on Ultrahydrophobic Surfaces and Its Effect on Droplet Mobility: Ultrahydrophobic Surfaces Are Not Always Water Repellant. *Langmuir* **2006**, *22*, 2433–2436. [CrossRef] [PubMed]

54. Li, H.; Li, Q.; Liu, H.; Wang, X.; Cao, K.; Li, J.; Zhang, B.; Yuan, W. Ice-resistant surface with three dimensional spherical halloysite aerogel: Construction and anti-icing mechanism. *Ceram. Int.* **2021**, *47*, 22976–22984. [CrossRef]

55. Golovin, K.; Kobaku, S.P.R.; Lee, D.H.; DiLoreto, E.T.; Mabry, J.M.; Tuteja, A. Designing durable icephobic surfaces. *Sci. Adv.* **2016**, *2*, e1501496. [CrossRef]

56. Lazauskas, A.; Guobienė, A.; Prosyčevas, I.; Baltrušaitis, V.; Grigaliūnas, V.; Narmontas, P. Water droplet behavior on superhy-drophobic SiO2 nanocomposite films during icing/deicing cycles. *Mater. Charact.* **2013**, *82*, 9–16. [CrossRef]

57. Kulinich, S.A.; Farhadi, S.; Nose, K.; Du, X.W. Superhydrophobic Surfaces: Are They Really Ice-Repellent? *Langmuir* **2010**, *27*, 25–29. [CrossRef]

58. Tian, X.; Verho, T.; Ras, R.H.A. Moving superhydrophobic surfaces toward real-world applications. *Science* **2016**, *352*, 142–143. [CrossRef]

59. Farhadi, S.; Farzaneh, M.; Kulinich, S. Anti-icing performance of superhydrophobic surfaces. *Appl. Surf. Sci.* **2011**, *257*, 6264–6269. [CrossRef]

60. Boinovich, L.B.; Emelyanenko, A.M.; Ivanov, V.K.; Pashinin, A.S. Durable Icephobic Coating for Stainless Steel. *ACS Appl. Mater. Interfaces* **2013**, *5*, 2549–2554. [CrossRef]

61. Ensikat, H.J.; Schulte, A.J.; Koch, K.; Barthlott, W. Droplets on Superhydrophobic Surfaces: Visualization of the Contact Area by Cryo-Scanning Electron Microscopy. *Langmuir* **2009**, *25*, 13077–13083. [CrossRef]

62. Feng, L.; Yan, Z.; Shi, X.; Sultonzoda, F. Anti-icing/frosting and self-cleaning performance of superhydrophobic aluminum alloys. *Appl. Phys. A* **2018**, *124*, 142. [CrossRef]

63. Shin, J.; Tikhonov, A.V.; Kim, C. Experimental Study on Frost Structure on Surfaces With Different Hydrophilicity: Density and Thermal Conductivity. *J. Heat Transf.* **2003**, *125*, 84–94. [CrossRef]

64. Gaddam, A.; Sharma, H.; Karkantonis, T.; Dimov, S. Anti-icing properties of femtosecond laser-induced nano and multiscale topographies. *Appl. Surf. Sci.* **2021**, *552*, 149443. [CrossRef]

65. Mohammadian, B.; Annavarapu, R.K.; Raiyan, A.; Nemani, S.K.; Kim, S.; Wang, M.; Sojoudi, H. Delayed Frost Growth on Nanoporous Microstructured Surfaces Utilizing Jumping and Sweeping Condensates. *Langmuir* **2020**, *36*, 6635–6650. [CrossRef] [PubMed]

66. Wang, T.; Zheng, Y.; Raji, A.-R.O.; Li, Y.; Sikkema, W.K.A.; Tour, J.M. Passive Anti-Icing and Active Deicing Films. *ACS Appl. Mater. Interfaces* **2016**, *8*, 14169–14173. [CrossRef] [PubMed]

67. Hao, J.-H.; Wang, Z.-J. Modeling Cassie–Baxter State on Superhydrophobic Surfaces. *J. Dispers. Sci. Technol.* **2015**, *37*, 1208–1213. [CrossRef]

68. Cassie, A.B.D.; Baxter, S. Wettability of porous surfaces. *Trans. Faraday Soc.* **1944**, *40*, 546–551. [CrossRef]

69. Nguyen, T.-B.; Park, S.; Jung, Y.; Lim, H. Effects of hydrophobicity and lubricant characteristics on anti-icing performance of slippery lubricant-infused porous surfaces. *J. Ind. Eng. Chem.* **2018**, *69*, 99–105. [CrossRef]

70. Chen, J.; Liu, J.; He, M.; Li, K.; Cui, D.; Zhang, Q.; Zeng, X.; Zhang, Y.; Wang, J.; Song, Y. Superhydrophobic surfaces cannot reduce ice adhesion. *Appl. Phys. Lett.* **2012**, *101*, 111603. [CrossRef]

71. Zheng, H.; Chang, S.; Ma, G.; Wang, S. Anti-icing performance of superhydrophobic surface fabricated by femtosecond laser composited dual-layers coating. *Energy Build.* **2020**, *223*, 110175. [CrossRef]

72. Boinovich, L.B.; Emelyanenko, K.A.; Emelyanenko, A.M. Superhydrophobic versus SLIPS: Temperature dependence and the stability of ice adhesion strength. *J. Colloid Interface Sci.* **2021**, *606*, 556–566. [CrossRef]

73. Vercillo, V.; Tonnicchia, S.; Romano, J.; García-Girón, A.; Aguilar-Morales, A.I.; Alamri, S.; Dimov, S.S.; Kunze, T.; Lasagni, A.F.; Bonaccurso, E. Design Rules for Laser-Treated Icephobic Metallic Surfaces for Aeronautic Applications. *Adv. Funct. Mater.* **2020**, *30*, 1910268. [CrossRef]

74. Metya, A.K.; Singh, J.K. Ice adhesion mechanism on lubricant-impregnated surfaces using molecular dynamics simulations. *Mol. Simul.* **2018**, *45*, 394–402. [CrossRef]

75. Elzaabalawy, A.; Meguid, S.A. Development of novel icephobic surfaces using siloxane-modified epoxy nanocomposites. *Chem. Eng. J.* **2021**, *433*, 133637. [CrossRef]

76. Li, X.Y.; Zhao, S.P.; Hu, W.H.; Zhang, X.; Pei, L.; Wang, Z. Robust superhydrophobic surface with excellent adhesive properties based on benzoxazine/epoxy/mesoporous SiO_2. *Appl. Surf. Sci.* **2019**, *481*, 374–378. [CrossRef]

77. Zheng, X.Q.; Pang, A.M.; Wang, Y.; Wang, W.; Bai, Y.P. Fabrication of UV-curable fluorosilicone coatings with impressive hydrophobicity and solvent resistance. *Prog. Org. Coat.* **2020**, *144*, 105633. [CrossRef]

78. Hussain, M.M.; Majeed, M.K.; Ma, H.T.; Wang, Y.P.; Saleem, A.; Lotfi, M. PTFE/EP Reinforced MOF/SiO_2 Composite as a Superior Mechanically Robust Superhydrophobic Agent towards Corrosion Protection, Self-Cleaning and Anti-Icing. *Chem. Eur. J.* **2022**, *28*, e202103220. [CrossRef]

79. Li, J.; Jiao, W.C.; Wang, Y.C.; Yin, Y.X.; He, X.D. Spraying pressure-tuning for the fabrication of the tunable adhesion super-hydrophobic coatings between Lotus effect and Petal effect and their anti-icing performance. *Chem. Eng. J.* **2022**, *434*, 134710. [CrossRef]

80. Yuan, S.; Zhao, X.; Jin, Z.Q.; Liu, N.Z.; Zhang, B.B.; Wang, L.F.; Duan, J.Z.; Hou, B.R. Fabrication of an environment-friendly epoxy coating with flexible superhydrophobicity and anti-corrosion performance. *Colloid Surface A* **2022**, *633*, 127545. [CrossRef]

81. Lu, W.G.; Zhang, S.G.; Wang, L.J.; Guo, C.Q.; Wang, X.; Wang, D.P.; Zhao, Z.B.; Yang, K.; Ma, Y.; Li, W.L. Understanding the role of epoxy emulsifiers in water-borne epoxy coatings with the aggregation-induced emission approach. *Prog. Org. Coat.* **2022**, *170*, 106987. [CrossRef]

82. Chen, X.Y.; Feng, Y.L.; Ma, Y.C.; Peng, S.S. A facile cathodic electrophoretic deposition (EPD) of GO nanosheet with an orderly layered nanostructure for development of long-term durability anticorrosive coating. *Prog. Org. Coat.* **2021**, *151*, 106034. [CrossRef]

83. Lu, Z.; Wang, J.Y.; Li, Q.; Chen, L.; Chen, S. Controllable synthesis of nanosilica surface-grafted PMMA macromonomers via catalytic chain transfer polymerization. *Eur. Polym. J.* **2009**, *45*, 1072–1079. [CrossRef]

84. Wang, S.Q.; Wang, Y.M.; Zou, Y.C.; Wu, Y.F.; Chen, G.L.; Ouyang, J.H.; Jia, D.C.; Zhou, Y. A self-adjusting PTFE/TiO_2 hydrophobic double-layer coating for corrosion resistance and electrical insulation. *Chem. Eng. J.* **2020**, *402*, 126116. [CrossRef]

85. Hu, Q.; Wang, S.J.; Yang, H.J.; Shu, L.C.; Jiang, X.L.; Li, H.T.; Qi, J.H.; Liu, Y.Q. Effects of icing degree on ice growth characteristics and flashover performance of 220 kV composite insulators. *Cold Reg. Sci.Technol.* **2016**, *128*, 47–56. [CrossRef]